

## ARTICLE OPEN



# Three-dimensional networks of superconducting NbSe<sub>2</sub> flakes with nearly isotropic large upper critical field

Togo Takahashi<sup>1,4</sup>, Chisato Ando<sup>2,4</sup>, Mitsufumi Saito<sup>3</sup>, Yasumitsu Miyata<sup>1,2</sup>, Yusuke Nakanishi<sup>1,2</sup>, Jiang Pu<sup>1</sup> and Taishi Takenobu<sup>1</sup>

Increasing the upper critical field  $H_{c2}$  in superconductors is one of the most significant requirements for superconducting applications. Two-dimensional (2D) noncentrosymmetric NbSe<sub>2</sub> is a promising candidate because its pair breaking is protected by the spin-momentum locking effect, resulting in a giant in-plane  $H_{c2}$  (~50 T). However, the strong anisotropy of 2D NbSe<sub>2</sub> suppresses the robustness of out-of-plane  $H_{c2}$  (<5 T). To overcome this issue, we propose a synthetic approach to produce superconducting NbSe<sub>2</sub> films with a nearly isotropic large  $H_{c2}$ . Scalable selenization methods are tailored to create 3D superconducting networks in which 2D NbSe<sub>2</sub> flakes are vertically aligned to the substrates. The angle-resolved magneto-transport reveals enhanced  $H_{c2}$  values that exceed 20 T for arbitrary directions under externally applied magnetic fields. The isotropic nature of  $H_{c2}$  is attributed to the averaging intrinsic anisotropy of NbSe<sub>2</sub> through 3D structured films, which was determined by X-ray diffraction measurements. The proposed synthetic approach will provide a new method for creating practical superconductors that are robust against magnetic fields.

npj 2D Materials and Applications (2021)5:31; <https://doi.org/10.1038/s41699-021-00210-7>

## INTRODUCTION

The upper critical field,  $H_{c2}$ , which is a magnetic field that completely destroys superconductivity, is a key physical parameter when designing robust superconducting device applications<sup>1,2</sup>. Materials for which noncentrosymmetry and spin-orbit interactions coexist, such as 2D superconducting NbSe<sub>2</sub>, may offer a higher-limit upper critical field strength and ameliorate the design constraints<sup>3,4</sup>. The geometric confinement of monolayers in 2D NbSe<sub>2</sub> allows a Zeeman-type spin-momentum (spin-valley) locking effect, and hence the resultant Ising pairing/superconductivity enables a giant in-plane  $H_{c2}$  ( $H_{c2}^{\parallel}$ ~50 T)<sup>5-15</sup>. In contrast, the  $H_{c2}$  for out-of-plane directions typically shows a much lower  $H_{c2}^{\perp}$  (~<5 T) than that of the in-plane directions, resulting in a strong anisotropic superconductivity in 2D NbSe<sub>2</sub><sup>5-13</sup>. Therefore, although NbSe<sub>2</sub> offers a possible robust superconductor against external magnetic fields, its significant anisotropy restricts its potential utility for future practical device designs.

The versatility of superconducting NbSe<sub>2</sub> can be expanded by realizing NbSe<sub>2</sub> films with isotropic, large  $H_{c2}$ . Specifically, these films would overcome the disparity issue between  $H_{c2}^{\parallel}$  and  $H_{c2}^{\perp}$ . One possible approach is to fabricate properly tailored 3D structures using nanoscale elements as building blocks<sup>16-18</sup>. Recently, a variety of 3D architectures have been created through the assembly of 2D materials<sup>19-24</sup>. For instance, the synthesis of vertically aligned MoS<sub>2</sub> films with high-density edges has enabled their use/application as efficient catalysts for hydrogen evolution<sup>20</sup>. In addition, Ajayan and Tiwary et al. created tough, ultralight 3D foam of graphene oxide with hexagonal boron nitride<sup>22</sup>. These successful bottom-up syntheses have inspired artificial 3D structures composed of 2D materials as an attractive platform to engineer new functionalities unavailable to the native 2D form<sup>23,24</sup>. Based on these ideas, we can expect that creating 3D networks of 2D superconducting NbSe<sub>2</sub> is a feasible way to

average the anisotropy of NbSe<sub>2</sub>. In particular, we hypothesize that the 3D structures with random orientations of 2D flakes enable the mixed contributions of intrinsic  $H_{c2}^{\parallel}$  and  $H_{c2}^{\perp}$  for arbitrary magnetic field angles to generate isotropic large  $H_{c2}$ .

With this strategy, developing scalable and morphology-tunable synthetic methods for NbSe<sub>2</sub> films is necessary. Until now, relevant research on NbSe<sub>2</sub> has been mainly demonstrated by single-crystalline flakes produced through mechanical exfoliations<sup>5-9</sup>, chemical vapor deposition (CVD)<sup>10,11</sup>, and molecular beam epitaxy (MBE)<sup>12-15</sup>. Direct selenization methods have recently been established to synthesize wafer-scale superconducting NbSe<sub>2</sub> films<sup>25</sup>. Nevertheless, the creation of large-area uniform 3D structured films still remains a challenge. Here, we report the direct growth of vertically aligned NbSe<sub>2</sub> films with a nearly isotropic large  $H_{c2}$ . The proposed methods can systematically control the thickness of centimeter-scale films, the morphologies of which vary according to the thickness of the initial Nb films. X-ray diffraction measurements revealed 3D structured films with vertically aligned 2D NbSe<sub>2</sub> flakes. In these 3D network films, we conducted angle-resolved magneto-transport measurements and achieved an  $H_{c2}$  of NbSe<sub>2</sub> beyond 20 T for all directions of the external magnetic fields. The results will provide a versatile approach for producing highly robust NbSe<sub>2</sub> superconducting applications based on nanoscale synthetic structure control.

## RESULTS

### Fabrication of 3D structured NbSe<sub>2</sub> films

Figure 1a shows the selenization process of Nb films used to grow 3D NbSe<sub>2</sub> films (see details in Supplementary Fig. 1a). Gao et al. recently reported a similar approach to preparing superconducting NbSe<sub>2</sub> films with atomic-level thickness and smoothness<sup>25</sup>. Although their thicknesses are tunable by the growth conditions,

<sup>1</sup>Department of Applied Physics, Nagoya University, Nagoya, Japan. <sup>2</sup>Department of Physics, Tokyo Metropolitan University, Tokyo, Japan. <sup>3</sup>Department of Electrical Engineering, Tokyo Metropolitan University, Tokyo, Japan. <sup>4</sup>These authors contributed equally: Togo Takahashi, Chisato Ando. ✉email: [naka24ysk@gmail.com](mailto:naka24ysk@gmail.com); [jiang.pu@nagoya-u.jp](mailto:jiang.pu@nagoya-u.jp); [takenobu@nagoya-u.jp](mailto:takenobu@nagoya-u.jp)

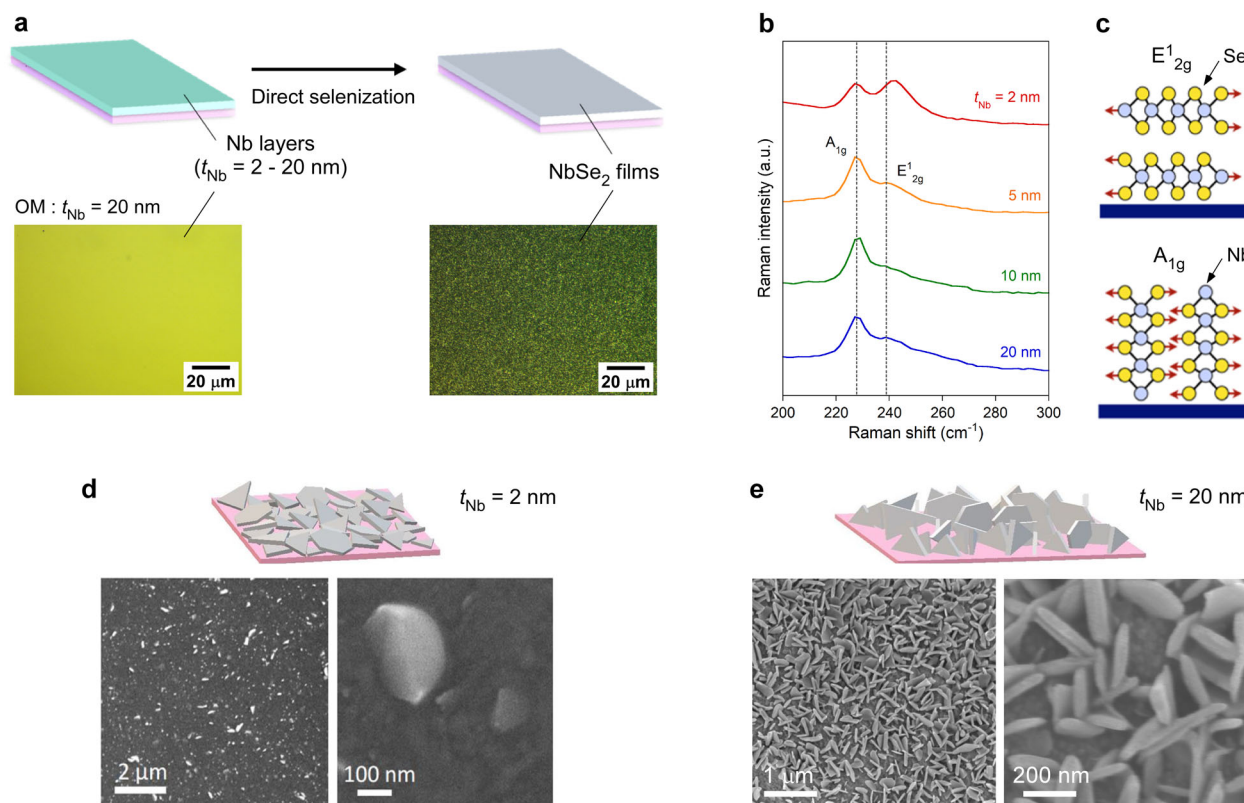


**Fig. 1 Growth and characterizations of large-area NbSe<sub>2</sub> films.** **a** A schematic illustration of the conversion from the deposited Nb films with the thickness,  $t_{\text{Nb}}$ , ranging from 2 to 20 nm, to the NbSe<sub>2</sub> films through the direct selenization process. Bottom: optical microscopic images of the Nb films on the SiO<sub>2</sub> substrates before and after vapor reactions for  $t_{\text{Nb}} = 20$  nm. **b** Raman spectra for the NbSe<sub>2</sub> films measured from precursor Nb films with different thicknesses. **c** Schematics of preferentially excited  $E_{2g}^1$  (top) and  $A_{1g}$  (bottom) Raman modes for the vertically stacked and aligned NbSe<sub>2</sub> films, respectively. **d, e** Low-magnified and high-resolution SEM images for NbSe<sub>2</sub> films with precursor Nb films of  $t_{\text{Nb}} = 2$  nm (**d**) and 20 nm (**e**), respectively. The top schematics illustrate the film morphology based on its corresponding SEM image. It is worth noting that the orientations (angles) of the vertically tilted NbSe<sub>2</sub> films are randomly embedded.

control over the morphologies of the films has yet to be investigated<sup>25,26</sup>. The bottom of Fig. 1a shows optical images of the as-deposited Nb films with  $t_{\text{Nb}} = 20$  nm and the selenized films on SiO<sub>2</sub>/Si substrates. The selenized films can be easily distinguished from the precursor Nb films by color. This selenization approach yielded wafer-scale uniform films (Supplementary Fig. 1b). It should be mentioned that the absence of unreacted Nb precursors and NbN films was confirmed through X-ray photoelectron spectroscopy (Supplementary Fig. 2). Figure 1b displays the Raman spectra of the selenide films generated from precursor Nb films of varying thicknesses, i.e.,  $t_{\text{Nb}} = 2, 5, 10,$  and 20 nm. All spectra exhibit two characteristic peaks within the range of 220–250 cm<sup>-1</sup>, which are assigned to the out-of-plane  $A_{1g}$  and in-plane  $E_{2g}^1$  phonon modes of NbSe<sub>2</sub>, respectively (Fig. 1c)<sup>27,28</sup>. A series of Raman spectra demonstrated the formation of NbSe<sub>2</sub> films regardless of the thickness of the initial Nb films.

Further Raman analyses also provided clues to the film morphologies. Except for the NbSe<sub>2</sub> films resulting from Nb films with  $t_{\text{Nb}} = 2$  nm (hereafter, this sample is called NbSe<sub>2</sub> ( $t_{\text{Nb}} = 2$  nm)), the three Raman spectra for other NbSe<sub>2</sub> samples ( $t_{\text{Nb}} \geq 5$  nm) exhibit consistent features, namely, the relative intensities between the two Raman modes ( $A_{1g} > E_{2g}^1$ ). According to an earlier study, the out-of-plane  $A_{1g}$  mode of vertical 2H-MoS<sub>2</sub> is preferentially excited when the excitation laser is irradiated perpendicular to the surface<sup>29</sup>. Indeed, the Raman spectra of vertically grown MoS<sub>2</sub> and MoSe<sub>2</sub> films show that the intensities of the  $A_{1g}$  peaks are stronger than those of the  $E_{2g}^1$  peak<sup>20</sup>. Layered NbSe<sub>2</sub> possesses the same hexagonal structure as 2H-MoS<sub>2</sub>, and

thus the reversed Raman signals suggest the formation of vertically aligned NbSe<sub>2</sub> films.

The formation of vertical NbSe<sub>2</sub> flakes in  $t_{\text{Nb}} \geq 5$  nm films was first confirmed by scanning electron microscopy (SEM). SEM images of NbSe<sub>2</sub> ( $t_{\text{Nb}} = 2$  and 20 nm) are shown in Fig. 1d and e, respectively. Figure 1d shows SEM images of polycrystalline NbSe<sub>2</sub> ( $t_{\text{Nb}} = 2$  nm) with relatively flat surfaces, similar to previously reported results. In contrast, on the surface of NbSe<sub>2</sub> ( $t_{\text{Nb}} = 20$  nm), triangular and hexagonal crystals were vertically grown with a grain size of 300–400 nm (Fig. 1e). Interestingly, the vertical NbSe<sub>2</sub> flakes were slightly tilted with a random orientation (random angles of each flake). Direct observation of the film surfaces indicates that the morphologies of NbSe<sub>2</sub> films are largely dependent on the thickness of the precursor Nb films, which is consistent with the Raman spectra in Fig. 1b (see also Supplementary Figs. 3–5 for further SEM and atomic force microscopy (AFM) observations).

### Structural characterization of 3D structured NbSe<sub>2</sub> films

The thickness-dependent morphologies, evaluated based on precursor Nb films of  $t_{\text{Nb}} = 2$ –20 nm, were further investigated using X-ray diffraction (XRD) measurements. Figure 2a and b shows representative 2D images of the XRD patterns of NbSe<sub>2</sub> films for  $t_{\text{Nb}} = 2$  nm (top) and  $t_{\text{Nb}} = 20$  nm (bottom). Figure 2c and d summarizes the peak profile recorded from the XRD patterns against the in-plane (Fig. 2c) and out-of-plane (Fig. 2d) directions on the substrates, respectively. The major peaks obtained at  $2\theta = 14^\circ$  and  $31^\circ$  are assigned to the (002) interlayer of the c-axis and intralayer (101) planes of NbSe<sub>2</sub> crystals, respectively, (the insets of Fig. 2c and d)<sup>30</sup>. For NbSe<sub>2</sub> ( $t_{\text{Nb}} = 2$  nm) shown in Fig. 2a and d, a

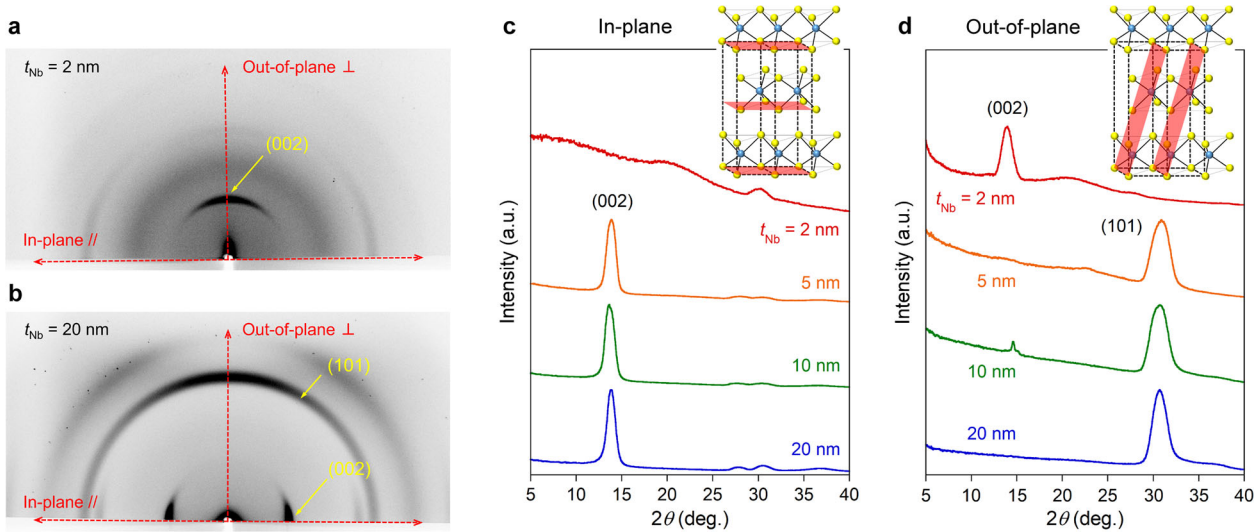


**Fig. 2** X-ray diffraction (XRD) characterization of NbSe<sub>2</sub> films. **a, b** The 2D image of XRD patterns recorded for as-prepared NbSe<sub>2</sub> films with precursor Nb films of  $t_{\text{Nb}} = 2$  nm (**a**) and 20 nm (**b**), respectively. **c, d** The peak profiles for XRD patterns of  $t_{\text{Nb}} = 2$ –20 nm, displayed for both in-plane (**c**) and out-of-plane directions (**d**) of the substrates. The insets of **c** and **d** show the unit cell of NbSe<sub>2</sub> crystals for interlayer (002) and intralayer (101) planes, respectively.

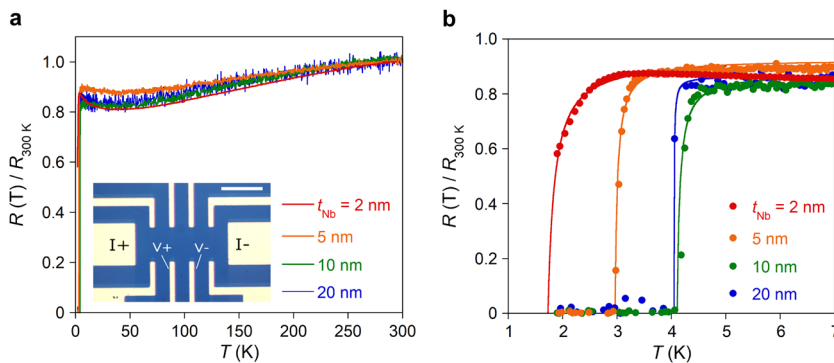


**Fig. 3** Superconductivity in large-area NbSe<sub>2</sub> films with varying precursor thickness. **a** Temperature dependence of electrical resistance,  $R$ , for NbSe<sub>2</sub> films of differing precursor thickness,  $t_{\text{Nb}} = 2$ –20 nm, in which the  $R$  is normalized by the value of  $R$  at 300 K ( $R/R_{300\text{K}}$ ). The inset shows an optical image of 4-terminal electrodes patterned on the surface of NbSe<sub>2</sub> films. The scale bar is 500  $\mu\text{m}$ . **b** Zoomed temperature dependence of  $R$  at lower temperatures. The superconducting transition is observed in all samples. Note that  $R$  does not show zero resistance in NbSe<sub>2</sub> ( $t_{\text{Nb}} = 2$  nm) because the measurement range was limited to 1.9 K. The solid lines indicate the fitting results using the Aslamazov-Larkin formula to determine  $T_C$ .

(002) reflection is strongly observed along the out-of-plane axis, suggesting that the films for  $t_{\text{Nb}} = 2$  nm consist of horizontally stacked NbSe<sub>2</sub> flakes (flat against the substrates). The  $d$  value for the (002) peaks was calculated as 0.64 nm, which is equivalent to half of the  $c$ -axis lattice constant of NbSe<sub>2</sub><sup>31</sup>. In contrast, the (002) peaks appeared primarily along the in-plane directions for NbSe<sub>2</sub> ( $t_{\text{Nb}} \geq 5$  nm), indicating vertically stacked NbSe<sub>2</sub> flakes on the substrates (Fig. 2b and c). Moreover, the (101) reflection for NbSe<sub>2</sub> films ( $t_{\text{Nb}} = 20$  nm in Fig. 2b) is broadly distributed along the Debye-Scherrer ring, suggesting that many NbSe<sub>2</sub> flakes are embedded with random orientations within the vertical films.

As shown in the series of in-plane and out-of-plane XRD patterns in Fig. 2c and d, the (002) peak is reduced with increasing  $t_{\text{Nb}}$  in the out-of-plane direction, whereas the (101) peak is enhanced, suggesting systematic control of film morphologies through the thickness of the initially deposited Nb films (see the detailed analysis for the XRD results in Supplementary Fig. 6). Importantly, these XRD patterns are consistent with the results of the Raman spectra and SEM images (Fig. 1b–e). Regarding the morphologies of NbSe<sub>2</sub> flakes, it should be noted that, whereas the 2D XRD patterns reveal a sharp contrast in the stacking nature

of NbSe<sub>2</sub> films between  $t_{\text{Nb}} = 2$  nm (horizontally shown in Fig. 1d) and  $t_{\text{Nb}} = 20$  nm (vertically shown in Fig. 1e), the (002) peak in both samples shows broad tail-like behaviors, meaning that many of the flakes are not completely flat ( $t_{\text{Nb}} = 2$  nm) or vertical ( $t_{\text{Nb}} = 20$  nm) against the substrates. This insight is also visible in the SEM images of Fig. 1d and e, that is, some NbSe<sub>2</sub> flakes are vertically aligned, but the others are randomly tilted to form 3D structured films (see Supplementary Fig. 5). Their vertical structures are significantly different from those of laterally grown NbSe<sub>2</sub> films<sup>25</sup>. The difference is probably due to a highly rough surface of the precursor Nb films, which were prepared through a faster deposition rate of  $\sim 0.5 \text{ nm s}^{-1}$  compared to the previous study ( $0.02 \text{ nm s}^{-1}$ )<sup>25</sup>. The rough surface of the precursor Nb films should be one of the key factors of the growth direction of NbSe<sub>2</sub> flakes, and the morphology should also be affected by the substrates.

### Electrical transport in large-area NbSe<sub>2</sub> films

To examine the electrical transport properties of NbSe<sub>2</sub> films, we conducted 4-terminal electrical resistance measurements (inset of Fig. 3a). Figure 3a shows the temperature ( $T$ ) dependence of the

electrical resistance,  $R$ , normalized by  $R$  at  $T = 300$  K ( $R/R_{300\text{K}}$ ) as measured for NbSe<sub>2</sub> ( $t_{\text{Nb}} = 2\text{--}20$  nm) under a zero magnetic field. The thin NbSe<sub>2</sub> film ( $t_{\text{Nb}} = 2$  nm) shows metallic behavior at higher temperatures, whereas at lower temperatures,  $R$  shows a slight increase, probably because of defects, localization effects, and/or scattering effects originating from grain boundaries<sup>10</sup>. In particular, the sharp drop in  $R$  at  $T < 3$  K indicates that the superconducting transition occurs. Because the measurement range was limited to 1.9 K, the sample did not reach zero resistance. For all thicker NbSe<sub>2</sub> films ( $t_{\text{Nb}} \geq 5$  nm), we obtained metallic behaviors and a significant decrease to zero resistance. Figure 3b shows the transport properties obtained at lower temperatures. Using the following Aslamazov-Larkin equation<sup>32</sup>, we determined the  $T_C$  for each sample:

$$R(T) = R_{\text{res}} \left( 1 - \frac{e^2 R_{\text{res}} T}{16\hbar T - T_C} \right) \quad (1)$$

where  $R_{\text{res}}$  is the residual resistance before the superconducting transitions,  $e$  is the elementary charge,  $\hbar$  is the reduced Planck constant, and  $T_C$  is the critical temperature for superconducting transitions. The  $T_C$  for the NbSe<sub>2</sub> films with  $t_{\text{Nb}} = 2, 5, 10,$  and  $20$  nm were found to be 1.61, 2.92, 4.06, and 4.04 K, respectively.

As shown in Fig. 3b, the changes in  $T_C$  from 1.6 to 4 K depending on the initial  $t_{\text{Nb}}$ . In most reported cases, the  $T_C$  of superconducting NbSe<sub>2</sub> strongly depends on the number of atomic layers, from single to few layered NbSe<sub>2</sub>, while  $T_C$  reaches up to 7.2 K for bulk NbSe<sub>2</sub><sup>5–13</sup>. The thickness dependence of  $T_C$  can be attributed to layer-to-layer interactions, substrate effects such as screening, and so on. Thus, we expect that variations in  $T_C$  in our samples may result from the cumulative effects of each individual flake's thickness within the synthesized films. To further confirm the thickness dependence of  $T_C$  in our samples, we used the Scherrer formula<sup>33</sup>,

$$\tau = \frac{K\lambda}{\beta \cos\theta} \quad (2)$$

where  $\tau$  is the mean size of the crystal domains,  $\lambda$  is the X-ray wavelength,  $\beta$  is the full width at half maximum, and  $K$  is the dimensionless shape factor used to estimate the thickness of the NbSe<sub>2</sub> flakes based on the XRD results (Fig. 2c and d). We focus on the (002) peaks to utilize the Scherrer formula, which directly provides the thickness of the individual flakes. The calculated  $\tau$  (with  $K = 0.9$ ) was 5.8, 6.5, 6.6, and 7.5 for NbSe<sub>2</sub> with  $t_{\text{Nb}} = 2, 5, 10,$  and  $20$  nm, respectively. Note that a similar flake thickness can also be observed from the detailed SEM image (see Supplementary Fig. 5). Because the  $c$ -axis lattice constant of NbSe<sub>2</sub> is  $\sim 1.3$  nm, which can be also derived from the  $d$  of (002) peak, the number of layers of the NbSe<sub>2</sub> flakes is estimated to range from 8 to 12<sup>31</sup>. Therefore, the measured differences in  $T_C$  resulting from changing the individual flake thickness agree qualitatively with the reported results<sup>5–13</sup>. The differences in the absolute values of  $T_C$  likely reflect the substrate effects, particularly for the NbSe<sub>2</sub> ( $t_{\text{Nb}} = 2$  nm) sample. Furthermore, the  $T_C$  of NbSe<sub>2</sub> ( $t_{\text{Nb}} = 20$  nm) represented a relatively low value because the thickness of 7.5 nm is close to the bulk limit, and its  $T_C$  should be higher than 4 K based on the reported results<sup>5</sup>. One possible reason for this result could be reflected in the smaller grain size of our films (200–300 nm) compared to that of the exfoliated samples (see the detailed SEM observations of Supplementary Fig. 5). These discrepancies may also result from the influences of defects, crystal disorders, and the grain orientation<sup>10</sup>. Indeed, the chemically grown polycrystalline NbSe<sub>2</sub> has a tendency to yield a lower  $T_C$ <sup>10,25</sup>. Although superconductivity was observed for all thicknesses and morphologies, further improvements and optimizations applied to synthesize high-quality polycrystalline films, such as a reduction in the moisture during growth, along with the effects of oxygen during the selenization process, could feasibly increase the amount of  $T_C$ .

### Magneto transport in 3D networks of NbSe<sub>2</sub> films

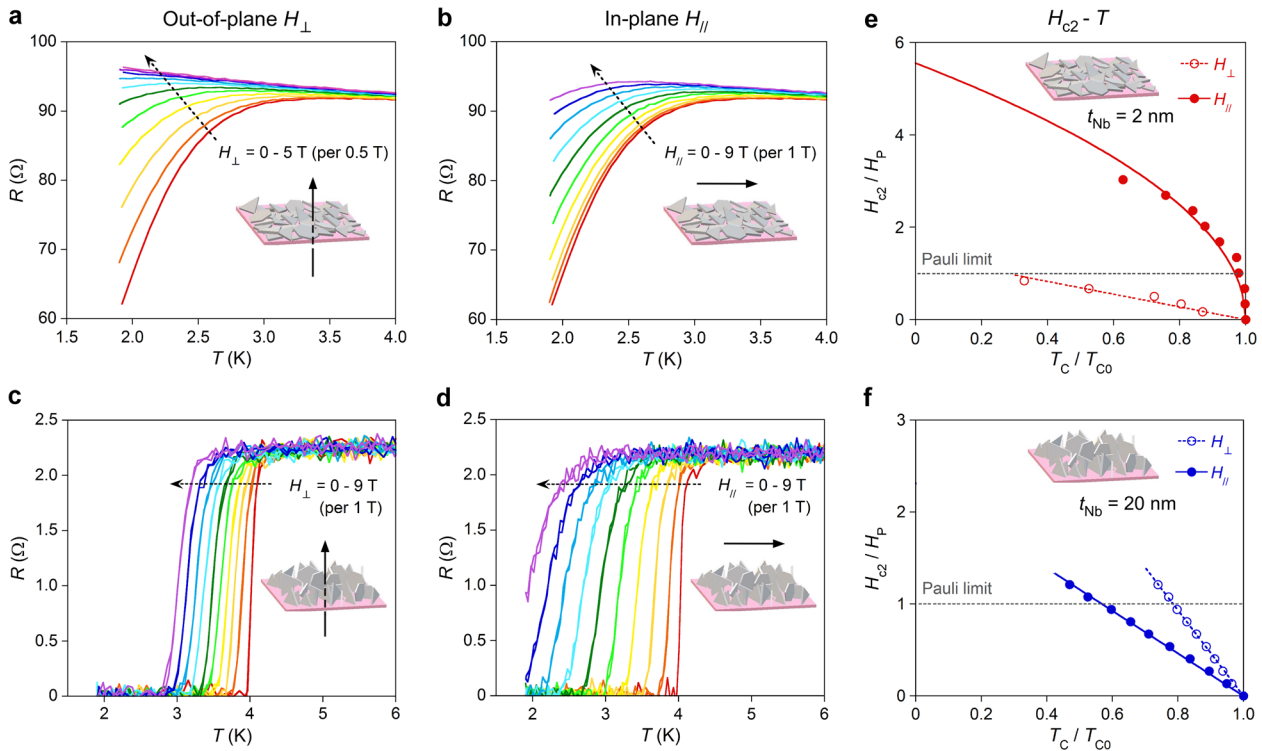
In addition to electrical transport measurements at zero magnetic fields, magneto-transport measurements can reveal important and relevant superconducting properties. In most superconductors, the pair-breaking process is dominated by both the orbital effect (limited by the cyclotron motion of electrons) and the paramagnetic effect (a Pauli-paramagnetic limit owing to the alignment of spin). Thus, extending the pair-breaking limit can produce an enhanced superconducting state that remains robust against external magnetic fields<sup>13,34,35</sup>. Because of the geometrical confinements of 2D NbSe<sub>2</sub>, the orbital effect is suppressed along the in-plane directions, resulting in anisotropic superconductivity. Particularly in the monolayer limit, the superconductivity of NbSe<sub>2</sub> is highly anisotropic owing to Ising pairing, which allows a drastic enhancement of the Pauli limit and yields a large in-plane  $H_{c2}$  ( $H_{c2}^{\parallel}$ ) arising from the spin-valley locking effect<sup>3–13</sup>. Conversely, the  $H_{c2}$  for out-of-plane directions is primarily dominated by the orbital effect, resulting in a lower  $H_{c2}^{\perp}$  than that of the Pauli limit. Considering the 2D superconducting nature of NbSe<sub>2</sub>, we proposed a strategy to enhance  $H_{c2}$  in all directions by synthesizing 3D structured films containing randomly oriented NbSe<sub>2</sub> flakes. These out-of-plane flakes collectively provide the film with a mixed contribution of  $H_{c2}^{\parallel}$  and  $H_{c2}^{\perp}$ , generating an averaged, large, and nearly isotropic  $H_{c2}$ . To prove this advantageous property, we directly compared the angle-resolved magneto-transport characteristics of NbSe<sub>2</sub> films between  $t_{\text{Nb}} = 2$  nm (horizontal) and 20 nm (vertical), linking their morphologies with the magnetic stability.

Figure 4a and b shows the value of  $R$  for NbSe<sub>2</sub> ( $t_{\text{Nb}} = 2$  nm) under field cooling by the out-of-plane magnetic fields  $H_{\perp}$  and in-plane fields  $H_{\parallel}$ , respectively. It should be noted that  $H_{\perp}$  and  $H_{\parallel}$  refer to the directions applied to the substrates (insets of Fig. 4a and b). Under  $H_{\perp}$ , the superconducting transition is mostly broken at  $\sim 3\text{--}4$  T, whereas under  $H_{\parallel}$ , the superconductivity survived up to 9 T. This magnetic response is equivalent to the reported results for atomically thin single-crystalline NbSe<sub>2</sub> films, and thus NbSe<sub>2</sub> ( $t_{\text{Nb}} = 2$  nm) is consistent with the horizontally aligned morphology (flat flakes against substrates)<sup>5–13</sup>. By contrast, the magnetic behavior of NbSe<sub>2</sub> ( $t_{\text{Nb}} = 20$  nm) shows an opposite response compared to that of NbSe<sub>2</sub> ( $t_{\text{Nb}} = 2$  nm). As shown in Fig. 4c and d, the superconductivity was more susceptible to  $H_{\parallel}$  in NbSe<sub>2</sub> films ( $t_{\text{Nb}} = 20$  nm), and was preserved even up to 9 T. Importantly, a robust superconducting state was achieved for both  $H_{\perp}$  and  $H_{\parallel}$ , which reflect an emerging property from the 3D film morphologies of out-of-plane NbSe<sub>2</sub> flakes grown on a flat substrate. These results agree well with the structural characterizations shown in Figs. 1 and 2. Similar behaviors were observed for samples with  $t_{\text{Nb}} = 5$  and 10 nm (Supplementary Fig. 7).

Figure 4e and f summarizes the  $H$ - $T$  phase diagrams for the samples at between  $t_{\text{Nb}} = 2$  and 20 nm (see supplementary Fig. 7 for the results of samples with  $t_{\text{Nb}} = 5$  and 10 nm). In thin NbSe<sub>2</sub> films ( $t = 2$  nm in Fig. 4e), strong anisotropy was obtained, and  $H_{c2}^{\parallel}$  far exceeded the Pauli limit of  $H_P \sim 1.84 T_C$ . Because  $T_C$  shows a linear response with  $H_{\perp}$ , it was fitted using the 2D Ginzburg-Landau equation based on orbital effects<sup>5,13</sup>,

$$\mu_0 H_{c2}^{\perp} = \frac{\Phi_0}{2\pi\xi^2} (1 - T/T_C) \quad (3)$$

where  $\Phi_0$  is the magnetic flux quantum, and  $\xi$  is the coherence length at zero temperature. In contrast, the  $T_C$ - $H_{\parallel}$  relationship showed a square root behavior; these results can be well explained using  $\mu_0 H_{c2}^{\parallel} \propto \sqrt{1 - T/T_C}$ , which incorporates the spin-momentum locking effect based on previous reports<sup>5</sup>. We should note that because the flake thickness of our samples (5–8 nm based on XRD results) was close to the bulk limit, the conventional 2D orbital effect would be also incorporated to obtain anisotropic behaviors. However, if we assume a pure orbital



**Fig. 4** Angle-resolved magneto transport in 3D structured NbSe<sub>2</sub> films. **a, b** The  $R$  of NbSe<sub>2</sub> films ( $t_{\text{Nb}} = 2$  nm) with field cooling displayed for the out-of-plane magnetic fields  $H_{\perp}$  (**a**) and in-plane  $H_{\parallel}$  (**b**). The inset illustrates the definitions of the applied magnetic fields. **c, d** The  $R$  of NbSe<sub>2</sub> films ( $t_{\text{Nb}} = 20$  nm) with field cooling exhibited for the  $H_{\perp}$  (**c**) and  $H_{\parallel}$  (**d**). **e, f** Comparison of  $H$ - $T$  phase diagrams for samples with  $t_{\text{Nb}} = 2$  nm (**e**) and 20 nm (**f**), representing both  $H_{\perp}$  and  $H_{\parallel}$ . The inset shows a schematic of the film morphologies. The black dotted line guides the Pauli limit of  $H_p \sim 1.84 T_C$ . Moreover, the colored solid and dotted lines indicate the square root and linear fitting for the experimental results, respectively.

effect,  $H_{c2}^{\parallel}$  should be far larger than the observed values. Therefore, we considered that both the conventional 2D effect and the spin-momentum locking effect coexisted to govern these anisotropic results, which qualitatively agrees with the reports on multilayer single-crystalline 2D flakes<sup>5</sup>. Therefore, we concluded that the superconducting properties were identical for each grain lying flat on the substrate, as indicated by Raman spectra, SEM images, and XRD patterns. Based on these analyses, the  $H_{c2}^{\parallel}$  reaches up to 45 T at zero temperature, which is slightly smaller than that of single-crystalline 2D flakes ( $\sim 50$  T)<sup>5–13</sup>. Moreover, the  $H_{c2}^{\perp}$  of NbSe<sub>2</sub> ( $t_{\text{Nb}} = 2$  nm) is slightly larger than the Pauli limit (Fig. 4e). These tendencies may stem from the incomplete horizontal alignment of the NbSe<sub>2</sub> flakes. As shown in Fig. 2a, the XRD patterns show broad behaviors of (002) peaks, indicating that the individual flakes are not totally flat and probably make a this slightly larger  $H_{c2}^{\perp}$  even in 2D NbSe<sub>2</sub> films.

In stark contrast to the strong anisotropic behavior in  $H_{c2}$  of the 2D form, the 3D NbSe<sub>2</sub> ( $t_{\text{Nb}} = 20$  nm) shown in Fig. 4f indicates distinct characteristics. If the 2D flakes simply stand vertically straight with the same orientations on the substrates, the  $H$ - $T$  relations should be inverted between 2D and 3D structures because the thicknesses of the individual flakes are mostly consistent based on the  $\tau$  values derived from the XRD. Interestingly, for both  $H_{c2}^{\parallel}$  and  $H_{c2}^{\perp}$ , the maximum  $H_{c2}$  values are beyond the Pauli limit, and linear  $H$ - $T$  relations are observed, in contrast to the results of 2D NbSe<sub>2</sub> ( $t_{\text{Nb}} = 2$  nm and the reported value). Thus, when we assume a linear behavior for  $H$ - $T$  relations,  $H_{c2}^{\parallel}$  can reach 18 T, and  $H_{c2}^{\perp}$  reaches 38 T at zero temperature. Moreover, these values are approximately one order of magnitude greater than those of  $H_{c2}^{\perp}$  in the relevant single-crystalline atomically thin NbSe<sub>2</sub> ( $< 5$  T). Because the NbSe<sub>2</sub> flakes are stacked vertically on the substrates, the larger  $H_{c2}^{\perp}$  than  $H_{c2}^{\parallel}$  in 3D

structured films is reasonable. However, the excess Pauli limit and linear  $H$ - $T$  relations for both  $H_{c2}^{\parallel}$  and  $H_{c2}^{\perp}$  cannot be explained only by the vertical characteristics of the 2D flakes, which suggests additional effects are required to yield a larger  $H_{c2}^{\perp}$  and  $H_{c2}^{\parallel}$ . Consequently, although we can realize a nearly isotropic large  $H_{c2}$  of  $> 18$  T ( $> 20$  T in Supplementary Fig. 7 for  $t_{\text{Nb}} = 5$  and 10 nm), indicating the enhanced magnetic stability of the 3D networks of NbSe<sub>2</sub> flakes, the origin of the improvement is not comprehensible by the simple standing of the 2D flakes. It is worth noting that a large  $H_{c2}$  was also maintained when changing the angles of the magnetic fields, supporting the isotropic performances of our samples (see Supplementary Fig. 8 for detailed  $H$ - $T$  relations at various magnetic field angles).

## DISCUSSION

Finally, we discuss the possible origin of the nearly isotropic enhancement of  $H_{c2}$  in synthetic 3D structured films. Comparing Fig. 4e and f, it is apparent that the  $H$ - $T$  relations (for both  $H_{\perp}$  and  $H_{\parallel}$ ) in 3D structured films fall between the  $H$  and  $T$  relations in the 2D form. Consequently, owing to their randomly oriented constituents, the 3D structures may be considered an averaged phenomenon of the intrinsic  $H_{c2}^{\parallel}$  and  $H_{c2}^{\perp}$  within individual 2D flakes. To evaluate this isotropic property, as shown in Fig. 5a, we compared the results measured from the 3D structured films to a recently reported angle-dependent  $H_{c2}$  in 2D single-crystalline NbSe<sub>2</sub> fabricated using MBE<sup>13</sup>. In the comparison study, the angle of the magnetic field was defined according to the orientation of the individual NbSe<sub>2</sub> flakes. Thus, for the sake of clarity, we will now refer to the  $H_{c2}^{\parallel}$  ( $H_{c2}^{\perp}$ ) substrate-specific directions described previously as  $H_{c2}^{\parallel}$  ( $H_{c2}^{\perp}$ ) flake-aligned directions, as in our 3D structured films. In a previous study of single-crystalline NbSe<sub>2</sub>

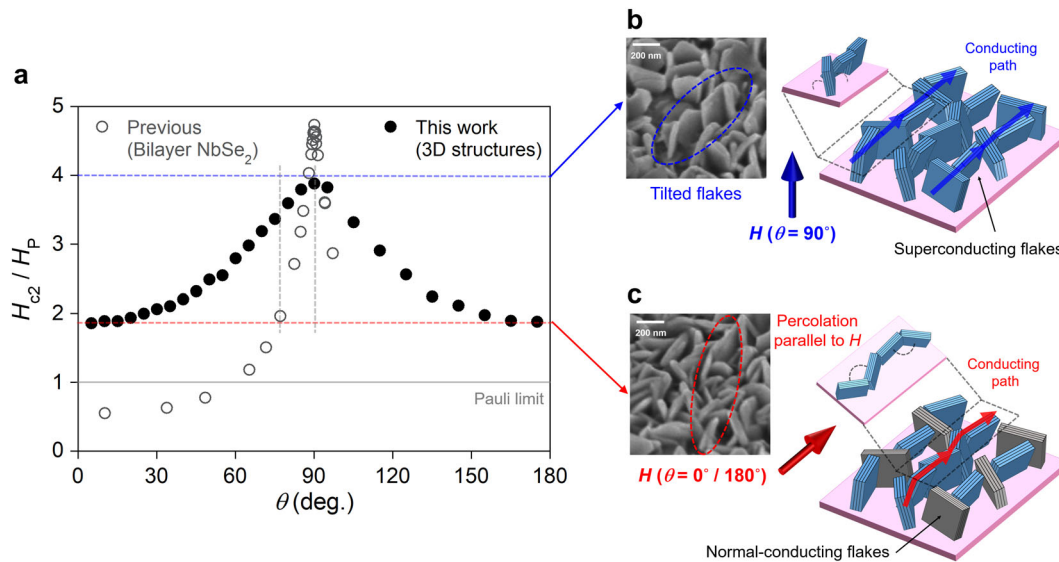


**Fig. 5** Nearly isotropic superconducting 3D networks of NbSe<sub>2</sub> films. **a** Comparison between our results of 3D structured films and reported angle-resolved  $H_{c2}$  in 2D (bilayer) NbSe<sub>2</sub> flakes fabricated using MBE<sup>13</sup>. To ensure a fair comparison, the value of  $H_{c2}$  derived from  $T_c/T_{c0} = 0.24$  was normalized using  $H_p$  ( $H_{c2}/H_p = 1$  displayed by the gray line). The maximum and minimum  $H_{c2}$  are denoted by the blue and red dotted lines, respectively. **b, c** Schematic showing distinct transport mechanism for yielding nearly isotropic large  $H_{c2}$ . When a magnetic field is applied to the out-of-plane directions of the substrates, the superconducting path is protected by vertically standing flakes (**b**). The inset of **b** shows a schematic and SEM image of 3D networks of the NbSe<sub>2</sub> films. The standing and tilted flakes create a robust superconducting path against a magnetic field of  $\theta = 90^\circ$ . By applying arbitrary angles of magnetic fields, the most robust superconducting path is automatically percolated to determine the total  $H_{c2}$ . When a magnetic field is applied to the in-plane directions of the substrates, the conduction path is created selectively by flakes parallel to the external magnetic field that protect the superconductivity, resulting in a large  $H_{c2}$  in all angles (**c**). The inset of **c** shows a schematic and an SEM image, in which the percolation of randomly oriented NbSe<sub>2</sub> flakes is generated parallel to the magnetic fields.

flakes, strong anisotropy was clearly observed (Fig. 5a), and thus the reported  $H_{c2}^\perp$  values are below the Pauli limit (owing to the orbital effect) and  $H_{c2}^\parallel$  values were greatly enhanced by the Ising pairing mechanism<sup>13</sup>. The crossover between the orbital limit and Pauli limit determines the total  $H_{c2}$  for different angles. In our 2D NbSe<sub>2</sub> ( $t_{\text{Nb}} = 2$  nm), the measured  $H_{c2}^\parallel$  and  $H_{c2}^\perp$  exhibit similar behaviors as relevant single-crystalline flakes, that is,  $H_{c2}^\perp$  is limited by the orbital limit, and  $H_{c2}^\parallel$  is enhanced with  $H_{c2}/H_p$  of  $\sim 5$  (Fig. 4e). However, in our 3D structured films, we observed larger  $H_{c2}$  values than the Pauli limit for all angles. We conclude that our nearly isotropic large  $H_{c2}$ , which improves the robustness of the overall superconductivity, originates purely from the new film morphologies.

The superconducting current within our 3D structured films can be understood as a collection of individual flakes that retain their superconductivity under an externally applied magnetic field and percolate throughout the larger 3D network to form a cohesive current path. If we were to apply an in-plane magnetic field higher than the  $H_{c2}^\perp$  for each flake, the standing flakes that were exactly perpendicular to the applied field would lose their superconductivity. However, because the standing flakes or “grains” are randomly oriented, such a field would not be perpendicular to the majority of the total grain surface. This allows the formation of flake-based current paths to preserve the superconductivity within the 3D structured films, suggesting that 3D morphologies suppress the relative angle dependence of the individual flakes and enable an enhanced isotropic  $H_{c2}$  for all angles. In fact, as shown in the XRD results of Fig. 2b, the intralayer (101) peaks appeared across the sequence of all angles, which directly suggests the existence of randomly oriented standing NbSe<sub>2</sub> flakes. Moreover, we found that the interlayer-related (002) peaks had slight tail behaviors at  $\sim 15^\circ$  for the in-plane directions of the substrates. This feature implies that NbSe<sub>2</sub> flakes do not stand completely vertically, but also tilt at specific angles ( $15^\circ$ ).

To further emphasize the unique transport properties in our 3D networks of superconducting films, we focus on the difference between  $H_{c2}^\parallel$  and  $H_{c2}^\perp$  in our samples and reported results, which presents that the decrease from maximum  $H_{c2}$  to that of minimum one<sup>13</sup>. In Fig. 5a, the slightly lower  $H_{c2}^\perp$  in our 3D structured film compared to that of the reported single-crystalline NbSe<sub>2</sub> would be reflected in the tiled morphologies, meaning that it is difficult for our 3D NbSe<sub>2</sub> to form a superconductive path using only grains perfectly perpendicular to the substrate. Considering the variations in the angle-dependent maximum and minimum  $H_{c2}$ , our samples could correspond to the range of  $75^\circ$ – $85^\circ$  measured in single-crystalline NbSe<sub>2</sub> (gray dotted line in Fig. 5a). Figure 5b shows a schematic of the carrier transport models in our 3D NbSe<sub>2</sub> films for magnetic angles of  $\theta = 90^\circ$ . When an out-of-plane magnetic field is applied to the substrate, the field is effectively charged parallel to the standing flakes, and thus the superconducting current path is largely protected (Fig. 5b). The slight lowering of the maximum  $H_{c2}$  compared to that of single-crystalline samples might be due to the incomplete protection because the standing flakes are tilted by  $\sim 15^\circ$  from vertical magnetic fields (the inset of Fig. 5b). Indeed, the  $H_{c2}$  within the angle range of  $90^\circ \pm 15^\circ$  showed small deviations against the magnetic fields owing to the tilted nature (see Supplementary Fig. 8).

Alternatively, when an in-plane magnetic field was applied to the substrate, the randomly oriented flakes generated the most robust superconducting path possible, which was percolated by the flakes standing parallel to the external magnetic field and yielded a large  $H_{c2}$  (Fig. 5c). Because the standing flakes were randomly oriented, the percolated flakes inevitably collected some portions of the weak superconducting path, that is, the percolated flakes were involved with specific angles against applied magnetic fields, resulting in an imperfect protection of the superconductivity (the inset of Fig. 5c). Under arbitrary magnetic field directions, the suitable percolating current paths act naturally to protect the superconductivity, thus achieving a nearly isotropic large  $H_{c2}$  for

all magnetic angles. We also compared the calculated and experimental results for angle-dependent  $H_{c2}$  based on the Ginzburg-Landau theory, and found that the experimental behaviors agreed well with the combination of  $H_{c2}^{\parallel}$  and  $H_{c2}^{\perp}$  arising from the 3D film morphologies (Supplementary Fig. 9). This mechanism is consistent with the SEM images shown in Fig. 1d and e (and Supplementary Fig. 5), and thus supports our synthetic strategy for the design of robust superconducting NbSe<sub>2</sub> films through 3D tailoring.

In summary, we established scalable selenization methods to synthesize 3D networks of NbSe<sub>2</sub> for robust superconducting films. The morphologies of large-area NbSe<sub>2</sub> films can be easily tuned through a two-step vapor-phase reaction of the initial thickness of the evaporated Nb films. Raman, SEM, and XRD characterization revealed 3D structured films consisting of out-of-plane flakes with random orientations. Angle-resolved magneto-transport measurements demonstrated an enhanced  $H_{c2}$  of 20–38 T for all directions of externally applied magnetic fields. The nearly isotropic nature of this large  $H_{c2}$  is attributed to the averaging of the intrinsic anisotropy of 2D NbSe<sub>2</sub> flakes and to the automatic selection of a robust current path owing to the 3D network of superconducting films. This proposed synthetic approach provides a powerful method for utilizing atomically thin superconducting materials for creating practical superconductors that can operate under high magnetic fields.

## METHODS

### Fabrication of 3D structured NbSe<sub>2</sub> films

Nb (99% purity, Nilaco Co.) was first deposited on SiO<sub>2</sub>/Si substrates using a vacuum deposition system (ULVAC, EX-200). The deposition was typically conducted under 10<sup>-4</sup> Pa with an evaporation rate of ~0.5 nm/s. Subsequently, the selenization process was carried out in a two-zone furnace under ambient pressure, where a mixture of H<sub>2</sub>/N<sub>2</sub> (3% H<sub>2</sub>, 300 sccm) was used as the carrier gas. The as-deposited Nb films were first positioned in a quartz tube (φ30) at the center of an electric furnace (ARF-30KC, Asahi-rika Co., Ltd.), and an alumina boat containing an excess amount of Se powder (2 g, 99% purity, Sigma-Aldrich) was then placed upstream at the center of the furnace. After purging with H<sub>2</sub>/N<sub>2</sub> for 10 min, the Se powder was heated at 360 °C and the Nb films were heated to 800 °C for 20 min and held for another 1 h. The furnace was then turned off and cooled to room temperature.

### Material characterization

Raman scattering measurements were conducted using confocal Raman systems equipped with a microscope (Renishaw, inVia) at a 533-nm excitation. A ×100 microscope objective (numerical aperture, NA = 0.9) was used to focus the laser beam and collect scattered light. SEM imaging was conducted using a desktop SEM (Phenom ProX, Thermo Fisher Scientific, Inc.) and high-resolution SEM (JSM-7100F, JEOL and S-4800, Hitachi High-Tech Co.). AFM topographic images were acquired in tapping mode over the scanning area using a scanning probe microscope (SPM-9600, Shimadzu Co.).

### XRD experiments

Grazing-incidence X-ray diffraction measurements were conducted using a Rigaku FR-E Microfocus High Intensity X-ray generator system with a CuKα X-ray source (wavelength of 0.15418 nm), conducted at the High Intensity X-ray Diffraction Laboratory at Nagoya University. The XRD patterns were detected using an imaging plate for both the in-plane and out-of-plane diffractions. The XRD measurements were conducted at room temperature and collected for all samples with different Nb film thicknesses. The same samples were used for both electrical and magneto-transport measurements.

### Electrical and magneto-transport measurements

The 4-terminal electrical and magneto-transport measurements were conducted using a physical property measurement system (PPMS, Quantum Design, Inc.). The 4-terminal Au/Ni (80 nm/2 nm) electrodes

were directly deposited on the surfaces of large-area NbSe<sub>2</sub> films (on Si/SiO<sub>2</sub> substrates). The channel width was 500 μm, and the channel length was 1000 μm, as shown in the inset of Fig. 3a. After wiring all contacts, the devices were placed inside the sample chamber under a He atmosphere. Following this, the temperature-dependent electrical resistance was measured using a current excitation of 100 nA. For angle-resolved magneto-transport measurements, a rotator was introduced to precisely control the angle of the substrate against an external magnetic field ranging from -9 to 9 T and a temperature of 300–1.9 K.

## DATA AVAILABILITY

All data that support the findings of this study are available from the corresponding authors upon request.

Received: 22 October 2020; Accepted: 16 February 2021;

Published online: 17 March 2021

## REFERENCES

- Yuan, H. Q. et al. Nearly isotropic superconductivity in (Ba,K)Fe<sub>2</sub>As<sub>2</sub>. *Nature* **457**, 565–568 (2009).
- Hahn, S. et al. 45.5-tesla direct-current magnetic field generated with a high-temperature superconducting magnet. *Nature* **570**, 496–499 (2019).
- Xu, X., Yao, W., Xiao, D. & Heinz, T.-F. Spin and pseudospins in layered transition metal dichalcogenides. *Nat. Phys.* **10**, 343–350 (2014).
- Saito, Y., Nojima, T. & Iwasa, Y. Highly crystalline 2D superconductors. *Nat. Rev. Mater.* **2**, 16094 (2017).
- Xi, X. et al. Ising pairing in superconducting NbSe<sub>2</sub> atomic layers. *Nat. Phys.* **12**, 139–143 (2016).
- Xi, X., Berger, H., Forro, L., Shan, J. & Mak, K. F. Gate tuning of electronic phase transitions in two-dimensional NbSe<sub>2</sub>. *Phys. Rev. Lett.* **117**, 106801 (2016).
- Ugeda, M. M. et al. Characterization of collective ground states in single-layer NbSe<sub>2</sub>. *Nat. Phys.* **12**, 92–97 (2016).
- Sohn, E. et al. An unusual continuous paramagnetic-limited superconducting phase transition in 2D NbSe<sub>2</sub>. *Nat. Mater.* **17**, 504–508 (2018).
- de la Barrera, S. C. et al. Tuning Ising superconductivity with layer and spin-orbit coupling in two-dimensional transition-metal dichalcogenides. *Nat. Commun.* **9**, 1427 (2018).
- Wang, H. et al. High-quality monolayer superconductor NbSe<sub>2</sub> grown by chemical vapour deposition. *Nat. Commun.* **8**, 394 (2017).
- Zou, Y.-C. et al. Superconductivity and magnetotransport of single-crystalline NbSe<sub>2</sub> nanoplates grown by chemical vapour deposition. *Nanoscale* **9**, 16591–16595 (2017).
- Xing, Y. et al. Ising superconductivity and quantum phase transition in macro-size monolayer NbSe<sub>2</sub>. *Nano Lett.* **17**, 6802–6807 (2017).
- Matsuoka, H. et al. Angle dependence of  $H_{c2}$  with a crossover between the orbital limit and paramagnetic limits. *Phys. Rev. Res.* **2**, 012064 (2020).
- Onishi, S. et al. Selenium capped monolayer NbSe<sub>2</sub> for two-dimensional superconductivity studies. *Phys. Status Solidi B* **253**, 2396–2399 (2016).
- Hotta, T. et al. Molecular beam epitaxy growth of monolayer niobium diselenide flakes. *Appl. Phys. Lett.* **109**, 133101 (2016).
- Cao, A., Dickrell, P. L., Sawyer, W. G., Ghasemi-Nejhad, M. N. & Ajayan, P. M. Supercompressible foamlite carbon nanotube films. *Science* **310**, 1307–1310 (2005).
- Ozden, S. et al. Controlled 3D carbon nanotube structures by plasma welding. *Adv. Mater. Interfaces* **3**, 1500755 (2016).
- Ozden, S. et al. Bacteria as bio-template for 3D carbon nanotube architectures. *Sci. Rep.* **7**, 9855 (2017).
- Sudeep, P. M. et al. Covalently interconnected three-dimensional graphene oxide solids. *ACS Nano* **7**, 7034–7040 (2013).
- Kong, D. et al. Synthesis of MoS<sub>2</sub> and MoSe<sub>2</sub> films with vertically aligned layers. *Nano Lett.* **13**, 1341–1347 (2013).
- Gong, Y. et al. Graphene-network-backboned architectures for high-performance lithium storage. *Adv. Mater.* **25**, 3979–3984 (2013).
- Vinod, S. et al. Low-density three-dimensional foam using self-reinforced hybrid two-dimensional atomic layers. *Nat. Commun.* **5**, 4541 (2014).
- Shehzad, K., Xu, Y., Gao, C. & Duan, X. Three-dimensional macro-structures of two-dimensional nanomaterials. *Chem. Soc. Rev.* **45**, 5541–5588 (2016).
- Chen, P.-Y., Liu, M., Wang, Z., Hurt, R. H. & Wong, I. Y. From flatland to spaceland: higher dimensional patterning with two-dimensional materials. *Adv. Mater.* **29**, 1605096 (2017).
- Lin, H. et al. Growth of environmentally stable transition metal selenide films. *Nat. Mater.* **18**, 602–607 (2019).

26. Park, S. et al. Tailoring domain morphology in monolayer NbSe<sub>2</sub> and W<sub>x</sub>Nb<sub>1-x</sub>Se<sub>2</sub> heterostructures. *ACS Nano* **14**, 8784–8792 (2020).
27. Tsang, J. C., Smith, J. E. Jr. & Shafer, M. W. Raman spectroscopy of soft modes at the charge-density-wave phase transition in 2H-NbSe<sub>2</sub>. *Phys. Rev. Lett.* **37**, 1407 (1976).
28. Wu, Y., An, M., Xiong, R., Shi, J. & Zhang, Q. M. Raman scattering spectra in the normal phase of 2H-NbSe<sub>2</sub>. *J. Phys. D Appl. Phys.* **41**, 175408 (2008).
29. Verble, J. L. & Wieting, T. J. Lattice mode degeneracy in MoS<sub>2</sub> and other layer compounds. *Phys. Rev. Lett.* **25**, 362 (1970).
30. Shi, Q. et al. Synergetic effect of NbSe<sub>2</sub> and Cr<sub>2</sub>Nb on the tribological and electrical behavior of Cu-based electrical contact composites. *RSC Adv.* **5**, 100472–100481 (2015).
31. Li, H. et al. Atomic structures and electronic properties of 2H-NbSe<sub>2</sub>: the impact of Ti doping. *J. Appl. Phys.* **116**, 103709 (2014).
32. Aslamasov, L. G. & Larkin, A. I. The influence of fluctuation pairing of electrons on the conductivity of normal metal. *Phys. Lett. A* **26**, 238–239 (1968).
33. Patterson, A. L. The Scherrer formula for X-ray particle size determination. *Phys. Lett.* **56**, 978 (1939).
34. Saito, Y. et al. Superconductivity protected by spin-valley locking in ion-gated MoS<sub>2</sub>. *Nat. Phys.* **12**, 144–149 (2016).
35. Lu, J. M. et al. Evidence for two-dimensional Ising superconductivity in gated MoS<sub>2</sub>. *Science* **350**, 1353–1357 (2015).

## ACKNOWLEDGEMENTS

This work was supported by a grant (No. JPMJCR16F3 and JPMJCR17I5) from the CREST program of the Japan Science and Technology Agency (JST), and by Grants-in-Aids (No. 18K14088 and 20H02572 to Y.N., No. JP19K15383 and 20H05189 to J.P., No. JP18H01832 to Y.M., No. JP26102012, JP25000003, 19K22127, 20H05867, and 20H05664 to T.T.) from the Japan Society for the Promotion of Science (JSPS). J.P. acknowledges support from KONDO-ZAIDAN. Y.N. appreciates financial support from The Murata Science Foundation and JKA2020 and its promotion funds from KEIRIN RACE. We also appreciate Hiroko Mineki from JASCO International Co., Ltd for SEM imaging and Tatsuo Hikage from Nagoya University for XRD measurements.

## AUTHOR CONTRIBUTIONS

To.T. and C.A. equally contributed. C.A., Y.N., and Y.M. developed fabrication of the NbSe<sub>2</sub> films and conducted the material characterizations. To.T. and J.P. performed the XRD characterizations, electrical, and magneto-transport measurements. To.T.

also contributed to detailed SEM characterizations. C.A. and M.S. contributed to AFM and SEM measurements. To.T., J.P., and Ta.T. performed the data analysis and the calculation of superconducting properties. Y.N., Y.M., J.P., and Ta.T. conceived and designed the experiments. Y.N. and J.P. wrote the manuscript. All authors discussed the results and commented on the manuscript.

## COMPETING INTERESTS

The authors declare no competing interests.

## ADDITIONAL INFORMATION

**Supplementary information** The online version contains supplementary material available at <https://doi.org/10.1038/s41699-021-00210-7>.

**Correspondence** and requests for materials should be addressed to Y.N., J.P. or T.T.

**Reprints and permission information** is available at <http://www.nature.com/reprints>

**Publisher's note** Springer Nature remains neutral with regard to jurisdictional claims in published maps and institutional affiliations.



**Open Access** This article is licensed under a Creative Commons Attribution 4.0 International License, which permits use, sharing, adaptation, distribution and reproduction in any medium or format, as long as you give appropriate credit to the original author(s) and the source, provide a link to the Creative Commons license, and indicate if changes were made. The images or other third party material in this article are included in the article's Creative Commons license, unless indicated otherwise in a credit line to the material. If material is not included in the article's Creative Commons license and your intended use is not permitted by statutory regulation or exceeds the permitted use, you will need to obtain permission directly from the copyright holder. To view a copy of this license, visit <http://creativecommons.org/licenses/by/4.0/>.

© The Author(s) 2021